High-resolution electron-momentum spectroscopy of the valence orbitals of the iodine molecule

J. S. Zhu, J. K. Deng, and C. G. Ning*

Department of Physics, State Key Laboratory of Low-Dimensional Quantum Physics, Tsinghua University, Beijing 100084, People's Republic of China

(Received 31 March 2012; published 24 May 2012)

The valence orbitals of the iodine molecule (I_2) have been studied using the high-resolution electron-momentum spectroscopy at impact energies of 1200 and 600 eV. Experimental momentum distributions of outer valence orbitals were compared with the nonrelativistic, scalar relativistic, and spin-orbital relativistic calculations, as well as the relativistic pseudopotential calculation. The experimental cross-section ratios of $8J_g^{3/2}$ to $17J_g^{1/2}$, $8J_u^{3/2}$ to $16J_u^{1/2}$, and the electron-momentum profiles of orbital $16J_g^{1/2}$ clearly manifested the relativistic effects. In the inner valence region, the symmetry-adapted-cluster configuration-interaction theory was used to interpret the ionization spectrum and the electron-momentum distributions.

DOI: 10.1103/PhysRevA.85.052714 PACS number(s): 34.80.Gs

I. INTRODUCTION

Electron-momentum spectroscopy (EMS) [1–3], also called $(e, 2e)$ spectroscopy, is a unique technique for investigating the electronic structures and the electron impact ionization dynamics. Based on the kinetic complete measurement of the $(e, 2e)$ reaction, EMS can measure the binding energy spectra and the electron-momentum distributions for each orbital at the same time. After the pioneering work by Weigold and co-workers in 1984 [4], in which they first demonstrated the ability of EMS on probing the relativistic effects of the Xe $5p$ orbital, researchers in this field have shown intensive interest in studying relativistic effects with the EMS method [5–12]. However, the targets were mainly limited to heavy atoms due to the difficulties of calculating the relativistic effects in a molecule in the last century. The main obstacle has been overcome thanks to the enormous progress made on relativistic quantum chemical methods since the 1980s [13–17]. Recently, we have introduced the relativistic density functional theory (DFT) for calculating the momentum distributions of molecular targets [10–12].

The iodine molecule (I_2) is an important prototype sample for testing many molecular theories. The atomic number of iodine is 53, and relativistic effects play an important role in its electronic structure and properties. Recently, we reported the theoretical electron-momentum profiles of the valence orbitals of the I_2 molecule using the spin-orbital relativistic theory [10]. The theoretical results showed that relativistic effects have notable effects on the electron-momentum distributions of I_2. Our first attempt to measure the I_2 sample at that time was not successful due to the high corrosivity of the iodine vapor to the spectrometer.

The valence electronic structure of I_2 has been investigated by the He I photoelectron spectroscopy (PES) [18]. The spin-orbital splittings were clearly resolved. The x-ray PES reported by Salaneck *et al*. [19] and the He II PES reported by Bieri *et al*. up to 25 eV [20] have shown that there are complicated satellite peaks around 20 eV. The high-resolution threshold photoelectron spectrum of the iodine molecule in the region 9–14 eV was investigated using synchrotron radiation [21]. The first EMS work on I_2 was reported by Grisogono *et al*. [22]. However, due to the relative low-energy resolution and the low statistical accuracy, the relativistic effects on the momentum distributions were not investigated particularly.

In this work, we report the high-resolution electron-momentum distributions of the valence orbitals of I_2 at impact energies of 1200 and 600 eV. The experimental momentum profiles were compared with the nonrelativistic, scalar relativistic, and spin-orbital relativistic calculations, as well as the relativistic pseudopotential calculation using the DFT method with the hybrid Becke three-parameter Lee-Yang-Parr (B3LYP) functional [23]. The cross-section ratios of $8J_g^{3/2}$ to $17J_g^{1/2}$ and $8J_u^{3/2}$ to $16J_u^{1/2}$ revealed the detailed information of the spin-orbital relativistic effects of the iodine molecule. The complicated spectrum was observed in the inner valence region, which can be reproduced using the symmetry-adapted-cluster configuration-interaction (SAC CI) general-R method [24–26]. The calculated momentum distributions of satellite lines using SAC CI theory describe the main features of the experimental profiles quite well.

II. THEORETICAL AND EXPERIMENTAL DETAILS

EMS is based on the $(e, 2e)$ experiment, where the target atom or molecule is ionized by an incident electron with a high energy. The scattered and the knocked-out electrons are coincidently detected. The $(e, 2e)$ reaction can be described as

$$e_0 + M \rightarrow M^+ + e_1 + e_2. \quad (1)$$

With the energy conservation and momentum conservation, the binding energy ε and, in the binary encounter and plane-wave impulse approximation (PWIA) [1–3], the momentum p of the target electron can be determined through the known energy E_0 of the incident electron (momentum p_0), and the measured energies of the two outgoing electrons E_1 (momentum p_1) and E_2 (p_2). Our spectrometer takes the symmetric noncoplanar geometry in which the two outgoing electrons have nearly the same kinetic energies ($E_1 \approx E_2$) and the same polar angle θ ($\theta_1 = \theta_2 = 45^\circ$) [27–29]. Therefore, the momentum of the electron before being knocked out can be given through the azimuthal angle ϕ between the two outgoing

*ningcg@tsinghua.edu.cn

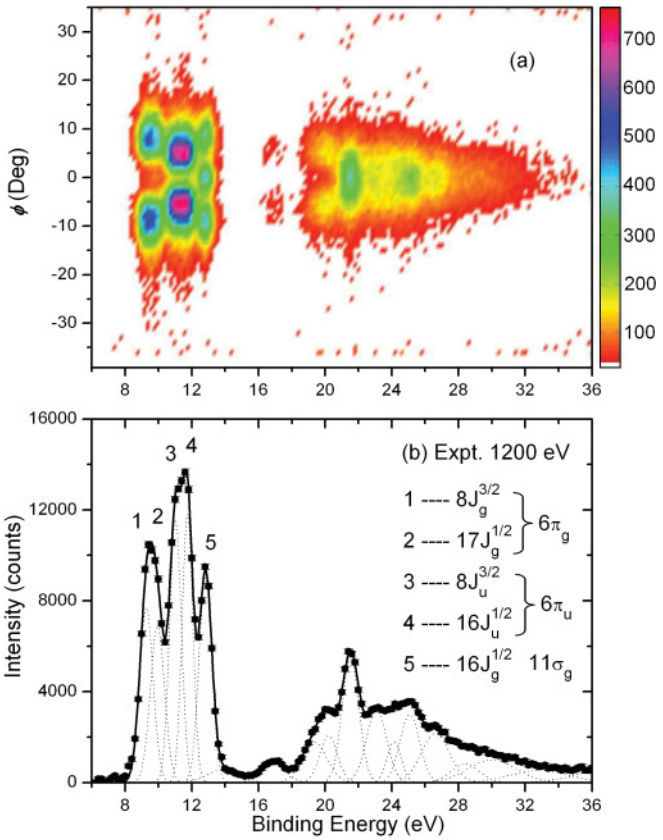

FIG. 1. (Color online) Binding energy spectra of I_2. (a) Momentum-energy density map of I_2 measured under the impact energy of 1200 eV. The intensity scale is shown by the color bar. (b) Experimental binding energy spectra summed over all azimuthal angles. The dashed and solid curves represent individual and summed Gaussian fits, respectively.

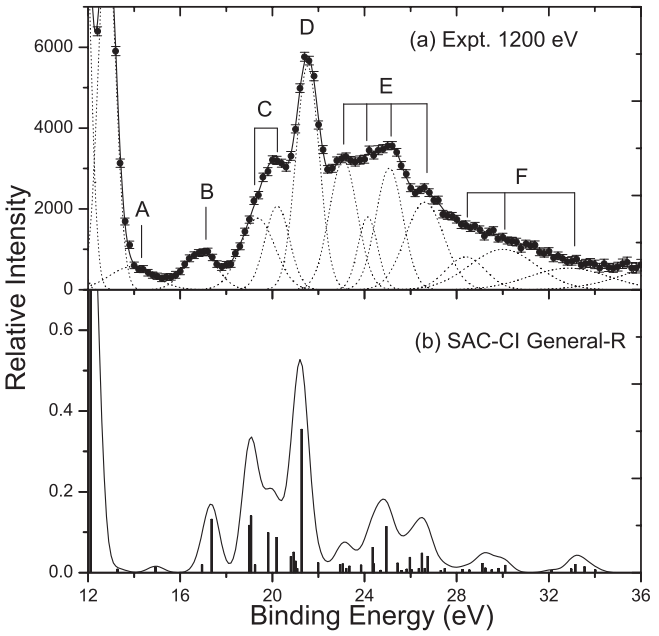

FIG. 2. Comparison of experimental and theoretical binding energy spectra of I_2 in the inner valence region. (a) Experimental binding energy spectrum of I_2 in the region 12–36 eV. (b) Simulated binding energy spectrum for I_2 using the SAC CI general-R method. The heights of short spikes represent the calculated spectroscopic factors.

electrons:

$$p = \left[(2p_1\cos\theta - p_0)^2 + 4p_1^2\sin^2\theta\sin^2\left(\frac{\phi}{2}\right)\right]^{1/2}. \quad (2)$$

Under the conditions of high impact energy and high-momentum transfer, the $(e, 2e)$ reaction can be well described with PWIA. The differential cross section for randomly oriented gas-phase target atoms or molecules is

$$\sigma_{\mathrm{EMS}} \propto S_i^f \int d\Omega \left|\left\langle e^{-ipr}\Psi_f^{N-1}\middle|\Psi_i^N\right\rangle\right|^2. \quad (3)$$

The differential cross section is proportional to the spectroscopic factor S_i^f. e^{-ipr} stands for the plane-wave function. $|\Psi_f^{N-1}\rangle$ and $|\Psi_i^N\rangle$ are the wave functions for the ionized state and the ground state of the target, respectively. $\langle\Psi_f^{N-1} \mid \Psi_i^N\rangle$ is also named the Dyson orbital. N is the total electron number. $\int d\Omega$ represents the spherical average over the random orientation of molecules. With the target Kohn-Sham approximation (TKSA) [30,31], the above equation can be simplified as

$$\sigma_{\mathrm{EMS}} \propto S_i^f \int d\Omega \left|\psi_j^{KS}(p)\right|^2, \quad (4)$$

where $\psi_j^{KS}(p)$ is the wave function of the jth electron in momentum space. As a result, EMS is able to image the individual orbitals in momentum space according to their binding energies.

Iodine ($Z = 53$) is a relatively heavy element. The relativistic effects of I_2 need to be carefully considered in the theoretical calculations. In the present work, the nonrelativistic, scalar relativistic, and spin-orbital relativistic calculations were performed using the full-electron triple-ζ doubly polarized basis set (TZ2P) via the zero-order regular approximation (ZORA) [32]. The calculations were implemented with the Amsterdam density functional (ADF) 2008 program [17,33]. The relativistic effects can also be partly taken into consideration through the relativistic pseudopotential. The DFT B3LYP and SAC CI general-R calculations using the augmented correlation-consistent polarized valence triple-zeta with pseudopotential (aug-cc-pvtz-pp) basis set for I [34] were also presented for comparison. The aug-cc-pvtz-pp basis set was taken from the basis set exchange website [35]. In the aug-cc-pvtz-pp basis set for I, the [Ar]$3d^{10}$ core was replaced using an energy-consistent relativistic pseudopotential [35].

SAC CI general-R theory is a reliable theory for the multiple excitation process. The calculations were performed using GAUSSIAN03 program [36]. The active space includes 96 molecular orbitals. The R operators up to quadruple were included. Perturbation selections were conducted to reduce the computation time. The threshold of the linked terms for the ground state was 1.0×10^6, and the unlinked terms were included as the products of the linked terms whose single- and double-configuration-interaction (SDCI) coefficients were larger than 5.0×10^{-3}. Since the I_2 belongs to the $D_{\infty h}$ point

TABLE I. Ionization potentials (IP) (eV) and spectroscopic factors (SF) of I_2.

	EMS[a]	PES[b]	SAC CI general-R[c]	ADC(4)[d]
1	9.28 (0.95)	9.31 ($8J_g^{3/2}$)	9.19 (0.881, $6\pi_g$)	9.33 (0.909, $6\pi_g$)
2	9.95 (0.95)	9.95 ($17J_g^{1/2}$)		
3	11.03 (0.81)	10.98 ($8J_u^{3/2}$)	11.14 (0.833, $6\pi_u$)	11.25 (0.865, $6\pi_u$)
4	11.75 (0.81)	11.82 ($16J_u^{1/2}$)		
5	12.82 (0.88)	12.95 ($17J_g^{1/2}$)	12.12 (0.856, $11\sigma_g$)	12.61 (0.833, $11\sigma_g$)
A	(0.10)			
	13.90		13.27 (0.008, $11\sigma_g$)	13.18 (0.066, $11\sigma_g$)
			14.93 (0.007, $6\pi_u$)	
B	(0.11)			
	16.88		16.95 (0.020, $10\sigma_g$)	16.66 (0.016, $10\sigma_g$)
			17.36 (0.068, $10\sigma_u$)	16.98 (0.138, $10\sigma_u$)
			17.38 (0.032, $6\pi_u$)	
C	(0.36)			
	19.36		18.98 (0.095, $10\sigma_u$)	18.54 (0.346, $10\sigma_u$)
	20.21			
			19.03 (0.011, $6\pi_g$)	18.88 (0.047, $10\sigma_u$)
			19.07 (0.140, $10\sigma_u$)	19.01 (0.018, $10\sigma_g$)
			19.25 (0.020, $10\sigma_g$)	19.76 (0.042, $10\sigma_u$)
			19.82 (0.099, $10\sigma_u$)	20.11 (0.027, $10\sigma_u$)
			20.18 (0.087, $10\sigma_u$)	20.14 (0.015, $6\pi_u$)
				20.24 (0.038, $10\sigma_u$)
D	(0.27)			
	21.53		20.81 (0.040, $10\sigma_u$)	20.67 (0.023, $10\sigma_u$)
			20.92 (0.025, $6\pi_u$)	21.37 (0.473, $10\sigma_g$)
			21.01 (0.028, $10\sigma_g$)	21.46 (0.010, $10\sigma_u$)
			21.07 (0.010, $10\sigma_u$)	22.04 (0.025, $10\sigma_u$)
			21.27 (0.355, $10\sigma_g$)	
			21.99 (0.024, $10\sigma_u$)	
E	(0.63)			
	23.08			
	24.14		22.94 (0.020, $10\sigma_g$)	23.15 (0.042, $10\sigma_g$)
	25.08			
	26.61			
			23.06 (0.021, $10\sigma_g$)	24.03 (0.081, $10\sigma_u$)
			23.21 (0.010, $10\sigma_g$)	24.94 (0.024, $10\sigma_u$)
			23.34 (0.016, $10\sigma_u$)	24.98 (0.010, $10\sigma_g$)
			23.85 (0.019, $10\sigma_u$)	25.32 (0.030, $10\sigma_g$)
			24.36 (0.062, $10\sigma_u$)	26.54 (0.010, $10\sigma_g$)
			24.41 (0.021, $10\sigma_g$)	26.75 (0.033, $10\sigma_g$)
			24.70 (0.005, $10\sigma_g$)	26.77 (0.036, $10\sigma_g$)
			24.95 (0.114, $10\sigma_u$)	27.35 (0.019, $10\sigma_g$)
			25.44 (0.023, $10\sigma_g$)	
			25.61 (0.005, $10\sigma_g$)	
			25.83 (0.008, $10\sigma_g$)	
			25.97 (0.038, $10\sigma_g$)	
			26.06 (0.006, $10\sigma_g$)	
			26.36 (0.010, $10\sigma_u$)	
			26.49 (0.048, $10\sigma_g$)	
			26.62 (0.010, $10\sigma_u$)	
			26.74 (0.040, $10\sigma_g$)	
			27.31 (0.005, $10\sigma_u$)	
			27.49 (0.010, $10\sigma_g$)	
F	(0.20)			
	28.39			
	30.01		28.26 (0.007, $10\sigma_g$)	30.31 (0.014, $10\sigma_u$)
	32.87			

TABLE I. (*Continued.*)

EMS[a]	PES[b]	SAC CI general-R[c]	ADC(4)[d]
		28.55 (0.006, $10\sigma_u$)	31.56 (0.013, $10\sigma_u$)
		29.12 (0.023, $10\sigma_g$)	31.93 (0.010, $10\sigma_g$)
		29.25 (0.011, $10\sigma_g$)	32.00 (0.011, $10\sigma_g$)
		29.53 (0.007, $10\sigma_g$)	32.31 (0.023, $10\sigma_g$)
		29.82 (0.010, $10\sigma_g$)	32.62 (0.011, $10\sigma_g$)
		30.11 (0.018, $10\sigma_g$)	
		32.12 (0.006, $10\sigma_g$)	
		32.97 (0.009, $10\sigma_g$)	
		33.15 (0.020, $10\sigma_g$)	
		33.55 (0.014, $10\sigma_g$)	
		34.02 (0.007, $10\sigma_g$)	

[a]This work. The values in the parentheses are the relative experimental spectroscopic factors.
[b]From Ref. [21]; the assignment based on the double group symmetry in the parentheses was given by this work.
[c]The spectroscopic factor and parent orbital of each Dyson orbital are given in the parentheses. We calculated 370 Dyson orbitals in total. Only these Dyson orbitals with a spectroscopic factor greater than 0.005 were listed here. Since each Dyson orbital is a linear combination of several tens of Hartree-Fock (HF) orbitals, we assign the HF orbital with the greatest absolute coefficient as its parent orbital.
[d]From Ref. [22].

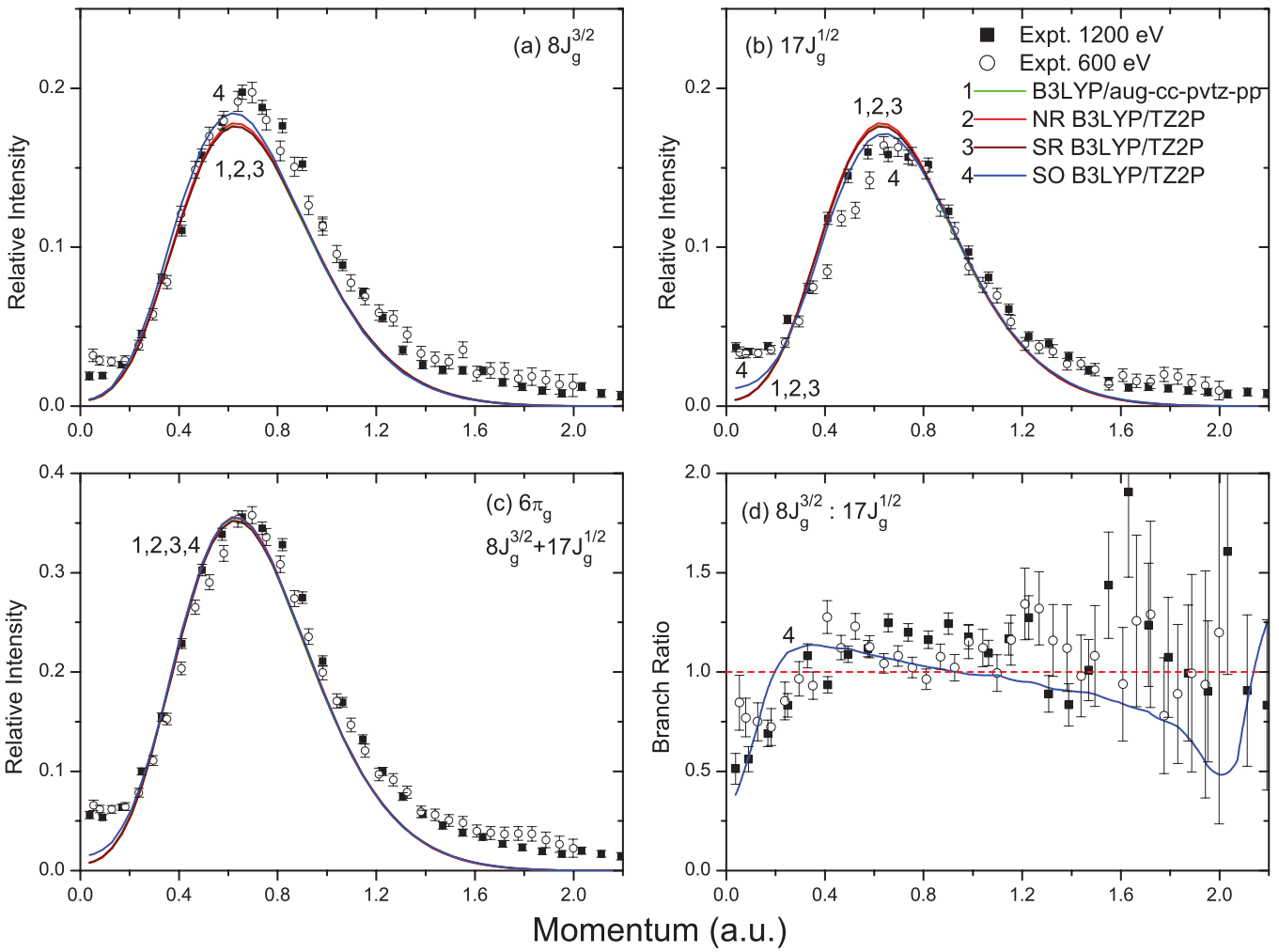

FIG. 3. (Color online) Momentum distributions of peak 1 and peak 2 of I_2. (a) Momentum distribution of $8J_g^{3/2}$; (b) momentum distribution of $17J_g^{1/2}$; (c) momentum distribution of $8J_g^{3/2} + 17J_g^{1/2}$; (d) cross-section ratio of $8J_g^{3/2}$ to $17J_g^{1/2}$ as a function of momentum. The red dashed line represents the nonrelativistic prediction. The error bars stand for one standard deviation. The experimental distributions are compared with the nonrelativistic (NR, curve 2), scalar relativistic (SR, curve 3), and spin-orbital relativistic (SO, curve 4) calculations. B3LYP aug-cc-pvtz-pp calculation (curve 1) includes a relativistic pseudopotential.

group, which has degenerated π orbitals, SAC CI calculations were implemented in its nondegenerated subgroup D_{2h}.

The details of our high-resolution spectrometer have been reported in previous works [27]. Briefly, the double toroidal energy analyzer equipped with the two-dimensional position-sensitive detectors is used to realize the energy and angle multichannel detection, which greatly enhances the sensitivity of the spectrometer. A specially designed electron gun with the oxide cathode can provide a collimated electron beam with a lower energy spread than the generic filament cathode. With the standard calibration run for the Ar $3p$ orbital, the present energy resolution was measured as $\Delta E = 0.7$ eV (full width at half maximum, FWHM) at the impact energy of 1200 eV, and it was slightly better at the impact energy of 600 eV. The azimuthal angle resolution is $\Delta\phi = \pm 0.84^\circ$ (one standard deviation), and the polar acceptance angle is $\Delta\theta = \pm 0.53^\circ$ [27]. The energy resolution may slightly deteriorate due to the long measuring period.

The commercial I_2 sample with a purity of 99.7% was directly used without further purification. It should be noted that the I_2 vapor reacts with most metal parts of our spectrometer. The contamination of the surfaces of the energy analyzer is even worse, which will distort the electron trajectories. As a result, the energy resolution will deteriorate. For this reason, the surfaces of the energy analyzer have been carefully coated with graphite. The relative low saturated vapor pressure of I_2 at room temperature and its high corrosivity make it inconvenient for controlling its gas target density at the collision region using the conventional needle valve outside the vacuum chamber. Instead, the I_2 sample was directly placed inside the spectrometer. The I_2 powder sample was sealed in a test tube, which has an outlet at one end. The outlet is a thin Teflon tube with an inner diameter of 0.2 mm and a length of 3 cm. The test tube was wrapped with a resistive heater. The background pressure in the vacuum chamber was $\sim 5 \times 10^{-5}$ Pa when the heater was off, and adjustable up to $\sim 4 \times 10^{-4}$ Pa by changing the heating power when the heater was on. This

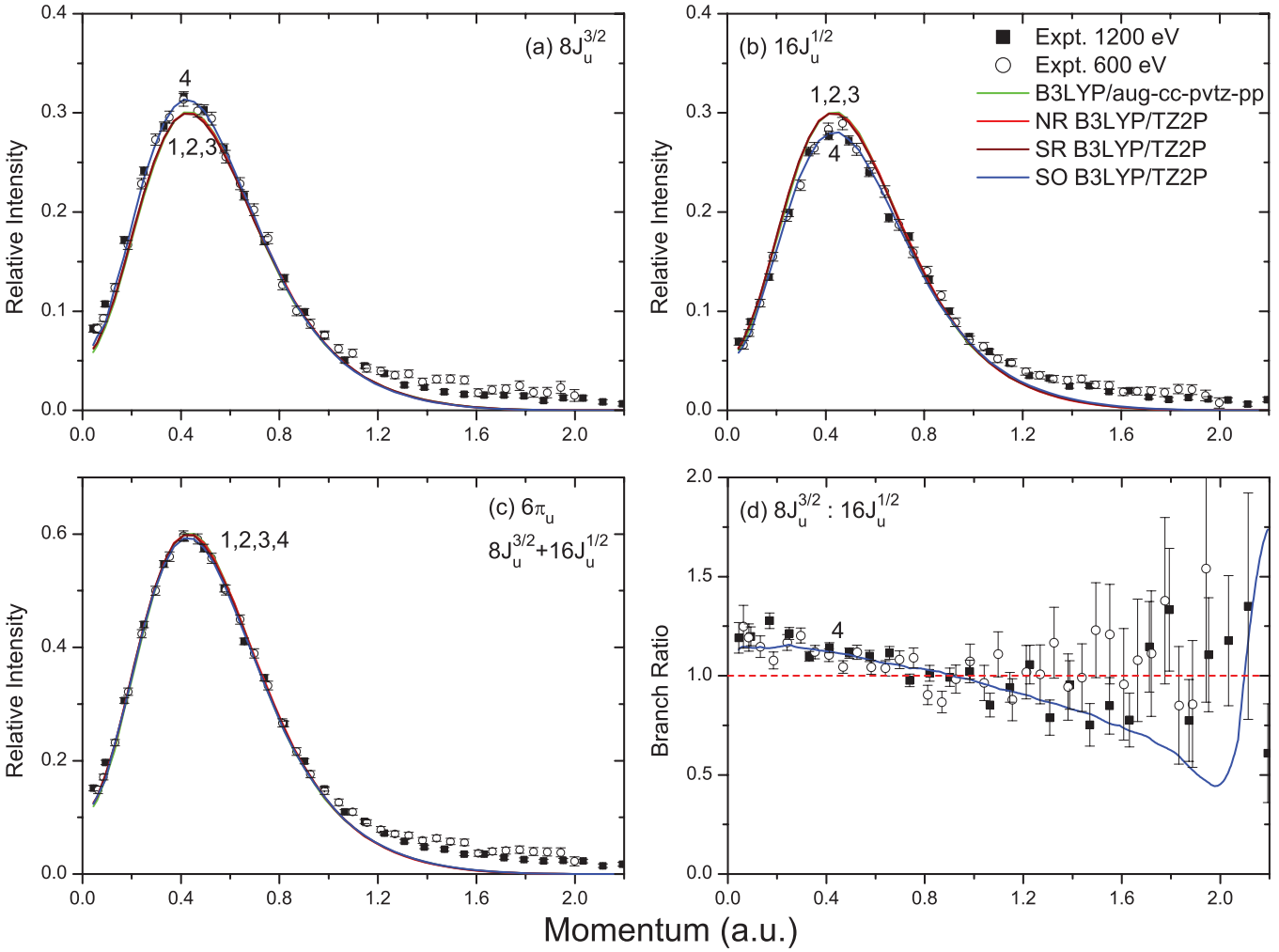

FIG. 4. (Color online) Momentum distributions of peak 3 and peak 4 of I_2. (a) Momentum distribution of $8J_u^{3/2}$; (b) momentum distribution of $16J_u^{1/2}$ as a function of momentum; (c) momentum distribution of $8J_u^{3/2} + 16J_u^{1/2}$; (d) cross-section ratio of $8J_u^{3/2}$ to $16J_u^{1/2}$. The red dashed line represents the nonrelativistic prediction. The experimental distributions are compared with the nonrelativistic (NR, curve 2), scalar relativistic (SR, curve 3), and spin-orbital relativistic (SO, curve 4) calculations. B3LYP aug-cc-pvtz-pp calculation (curve 1) includes a relativistic pseudopotential.

simple method could diminish the corrosion by controlling the vapor pressure when we were tuning the spectrometer and pumping down the vacuum. The valence orbitals of I_2 were successfully measured. However, as we tried to measure the I $4d$ core orbital, whose $(e, 2e)$ cross section is much smaller than that of the valence orbitals, the turbo pump of the spectrometer finally failed after having been exposed to the I_2 vapor for three weeks.

III. RESULTS AND DISCUSSION

A. Binding energy spectra of I_2

The iodine molecule contains 106 electrons and has $D_{\infty h}$ point-group symmetry. The index numbers of molecular orbitals are different when the calculation uses different frozen cores. In this work, the orbital assignment was unified to the calculations using the TZ2P basis set without a frozen core. The electronic configuration of I_2 in the single group representation can be written as

$$(\text{core})^{92}\underbrace{(10\sigma_g)^2(10\sigma_u)^2}_{\text{inner valence}}\underbrace{(11\sigma_g)^2(6\pi_u)^4(6\pi_g)^4}_{\text{outer valence}}.$$

According to the spin-orbital relativistic B3LYP TZ2P calculation in the double group symmetry [37], the ground state is

$$(\text{core})^{92}\underbrace{(15J_g^{1/2})^2(15J_u^{1/2})^2}_{\text{inner valence}} \times \underbrace{(16J_g^{1/2})^2(16J_u^{1/2})^2(8J_u^{3/2})^2(17J_g^{1/2})^2(8J_g^{3/2})^2}_{\text{outer valence}}.$$

The single group orbital $6\pi_g$ is split into $8J_g^{3/2}$ and $17J_g^{1/2}$, and $6\pi_u$ is split into $8J_{gu}^{3/2}$ and $16J_u^{1/2}$. The calculated energy splittings of orbitals $6\pi_u$ and $6\pi_g$ are 0.6 eV and 0.8 eV, respectively, in good agreement with the high-resolution photoelectron spectrum [21].

The observed momentum-energy density map of I_2 under the impact energy of 1200 eV plus the binding energies is shown in Fig. 1(a). There are three different features in the binding energy range 8–13.5 eV in the map, which are related to the $6\pi_g$, $6\pi_u$, and $11\sigma_g$ orbitals. To extract the momentum distribution for each orbital, the binding energy spectra at different azimuthal angles ϕ were fitted using Gaussian functions. The binding energy spectrum in Fig. 1(b) was obtained by summing over all the azimuthal angles. With reference to the high-resolution PES [18,21], five individual Gaussian peaks were used for fitting the binding energy spectra in the outer valence range (8–13.5 eV).

The complicated inner valence spectrum (13.5–36 eV), where 13 Gaussian peaks were used for fitting, cannot be interpreted with the single-particle DFT models. There are no distinct main peaks for the two inner valence orbitals $10\sigma_g$ and $10\sigma_u$ due to the severe breakup of the orbital picture. The expanded binding spectrum in the inner valence region was shown in Fig. 2(a), which was compared with the simulation using the SAC CI general-R method with the aug-cc-pvtz-pp basis set. It can be seen that the orbitals $10\sigma_g$ and $10\sigma_u$ break up into many congested satellite lines. The Gaussian peaks used for fitting the binding energy spectrum in this region were grouped into six bands (A–F). The SAC CI general-R calculation can reproduce most of the features of the binding energy spectrum. Since the SAC CI calculation cannot generate the spin-orbital splittings, it cannot well simulate the experimental binding energy spectrum in the outer valence region (8–13.5 eV).

B. Momentum distributions of outer valence orbitals

Since the experimental intensities are in the relative scale, the experimental normalization is needed to compare with the theoretical distributions. Here, the summed experimental distributions of peaks 1–5 were compared with the summation of the spin-orbital relativistic calculations in order to determine the common normalization constant. The Kohn-Sham orbitals have been multiplied by the theoretical spectroscopic factors given by SAC CI. Then the common normalization constant was used to determine the relative experimental spectroscopic factor for each outer valence orbital, as shown in Table I.

Figure 3 shows the electron-momentum distributions for $8J_g^{3/2}$ and $17J_g^{1/2}$ orbitals under impact energies of 1200 and 600 eV. The theoretical momentum profiles have been convolved with the experimental momentum resolution at the impact energy 1200 eV using a Monte Carlo method [38]. Generally, the relativistic pseudopotential (curve 1), the nonrelativistic (curve 2), the scalar relativistic (curve 3), and the spin-orbital relativistic (curve 4) calculations can reproduce the overall experimental profiles. The curves 1, 2, and 3 are almost identical, which are the calculated momentum distributions of $6\pi_g$ divided by 2. The spin-orbital relativistic calculation predicted a slightly different distribution of $8J_g^{3/2}$ from that of $17J_g^{1/2}$. Especially, there are discernable differences in the low-momentum region $p < 0.2$ a.u. and in the region around 0.6 a.u. The summed momentum distributions of $8J_g^{3/2}$ and $17J_g^{1/2}$ were also compared with the calculated ones in Fig. 3(c) because of the significant overlap

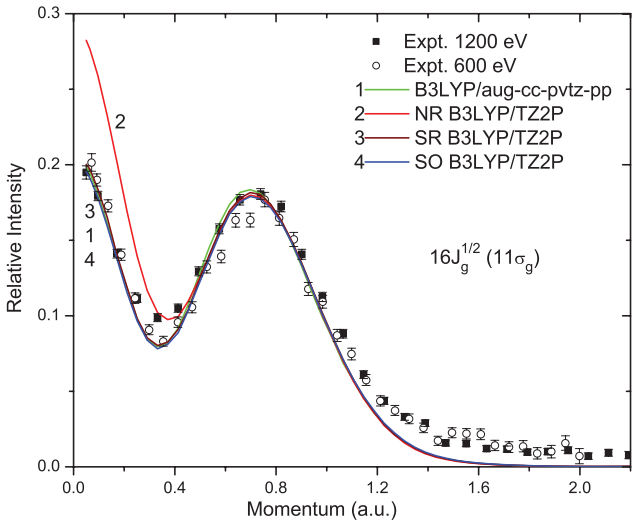

FIG. 5. (Color online) Momentum distributions of peak 5 of I_2. The experimental distributions are compared with the nonrelativistic (NR, curve 2), scalar relativistic (SR, curve 3), and spin-orbital relativistic (SO, curve 4) calculations. B3LYP aug-cc-pvtz-pp calculation (curve 1) includes a relativistic pseudopotential.

between the two peaks. In Figs. 3(a)–3(c), the calculations underestimated the experimental intensities of $8J_g^{3/2}$ and $17J_g^{1/2}$ orbitals in the low-momentum region $p < 0.2$ a.u. The similar phenomenon was also observed in the highest occupied molecular orbital (HOMO) of the oxygen molecule [39]. Both HOMOs of O_2 and I_2 are typical π^* orbitals. The observed "turnup" in the low-momentum region for d-like orbitals is usually attributed to the distorted wave effects [40]. Indeed, the discrepancies in Fig. 3(c) become smaller at 1200 eV than those at 600 eV, although not remarkably so, which is consistent with the explanation of the distorted wave effects. It is interesting to compare the experimental cross-section ratios of $8J_g^{3/2}$ to $17J_g^{1/2}$ with theoretical ratios without resorting to the normalization procedure, as shown in Fig. 3(d). Only the spin-orbital calculation can describe the branch ratio as a function of momentum. The other three calculations predicted a constant ratio 1.0, which is independent of the momentum.

The momentum distributions for $8J_u^{3/2}$ and $16J_u^{1/2}$ are shown in Figs. 4(a) and 4(b). The curves 1, 2, and 3 are the calculated momentum distributions of $6\pi_u$ divided by 2. All calculations can well describe the experimental distributions, and the spin-orbital relativistic calculation (curve 4) provided the best description. The summed momentum distributions of $8J_u^{3/2}$ and $16J_u^{1/2}$ were compared with theoretical calculations in Fig. 4(c). The theoretical results are in excellent agreement with the experimental distributions. Again, the experimental

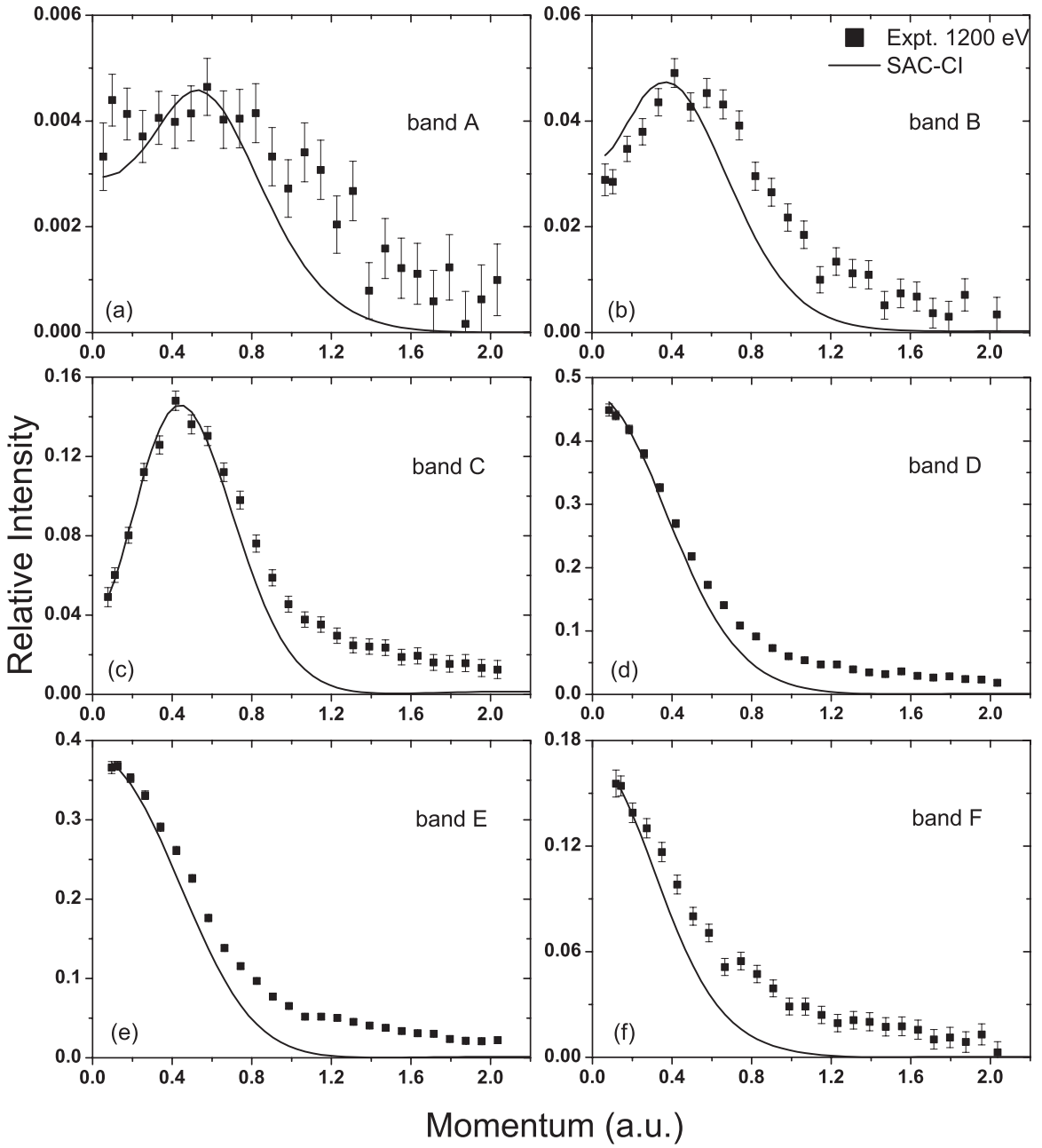

FIG. 6. Momentum distributions for bands A−F in the inner valence region of I_2. The experimental momentum distributions are compared with the calculated distributions using SAC CI general-R method with aug-cc-pvtz-pp basis set.

branch ratio of $8J_u^{3/2}$ to $16J_u^{1/2}$ was compared with the theoretical predictions, as shown in Fig. 4(d). Only spin-orbital relativistic calculation can well describe the observed results.

As shown in Fig. 5, the momentum profile of orbital $16J_g^{1/2}$ is sp type, which has a maxim at $p = 0$ a.u. and a hump at $p = 0.74$ a.u. The momentum profiles generated by scalar relativistic, spin-orbital relativistic, and pseudopotential (B3LYP-aug-cc-pvtz-pp) methods are nearly the same, and they are all consistent with the experimental distributions. But the nonrelativistic calculation highly overestimated the experimental intensity in the low-momentum region $p < 0.5$ a.u. Therefore, the relativistic effect on the electronic structure of I_2 is non-negligible.

C. Momentum distributions of inner valence orbitals

The single-particle models fail to interpret the details of the congested satellite lines in the inner valence region. In order to investigate the congested satellite lines in the inner valence region of I_2 (>13.5 eV), the SAC CI general-R method with the aug-cc-pvtz-pp basis set was used for interpreting the experimental results. Thirteen Gaussian peaks were used to fit the binding energy spectrum in this range in order to obtain their experimental momentum distributions. As these peaks are not well resolved, they were grouped into six bands (A–F), as shown in Fig. 2(b).

The ionization potentials and spectroscopic factors of these peaks are listed in Table I. In Fig. 6, the experimental momentum distributions of the six bands are compared with the calculated distributions by SAC CI general-R method. The main sources of band A are the satellite lines at 13.27 and those at 14.93 eV. The parent orbitals of satellite lines at 13.27 and 14.93 eV are $11\sigma_g$ (0.008) and $6\pi_u$ (0.007), respectively. The values in parentheses are the theoretical spectroscopic factors. As shown in Fig. 6(a), the theoretical momentum distributions generated by the above two Dyson orbitals can describe the profile of the experimental distribution. However, the predicted spectroscopic factor 0.022 ($0.008 + 2 \times 0.007$) is lower than the experimental value, which is determined as 0.10. The twofold degeneration of $6\pi_u$ has been considered. The spectroscopic factor for band A given by ADC(4) is 0.066, which is closer to the observed value, but the predicted contribution only from an s-type $11\sigma_g$ orbital cannot describe the observed distribution. Here, ADC(4) stands for the fourth-order algebraic diagrammatic construction scheme, which is a specific reformulation of the diagrammatic perturbation series of the electron propagator [41]. The theoretical momentum distribution for band B, which has mixed sources from $10\sigma_g$, $10\sigma_u$, and $6\pi_u$, can describe the experimental profile. The dominant source for band C is from $10\sigma_u$, which is the p-type orbital, as shown in Fig. 6(c). The dominant source for band D is from $10\sigma_g$, which is an s-type orbital. For band E, the contributions from $10\sigma_g$ and $10\sigma_u$ are mixed together. The main source for band F is from an s-type $10\sigma_g$ orbital.

IV. CONCLUSIONS

The experimental momentum distributions of the valence orbitals of the iodine molecule have been reported at impact energies of 1200 and 600 eV. The theoretical calculations using the nonrelativistic, scalar relativistic, and spin-orbital relativistic methods, as well as the relativistic pseudopotential method, were compared with the experimental results, which showed that relativistic effects have notable influence on the electron-momentum distributions of the iodine molecule. The SAC CI general-R method can well describe the binding energy spectrum and the electron-momentum distributions in the inner valence region.

ACKNOWLEDGMENT

This work was supported by the National Nature Science Foundation of China (Grants No. 11074144 and No. 11174175).

[1] I. E. McCarthy and E. Weigold, Rep. Prog. Phys. **54**, 789 (1991).
[2] M. A. Coplan, J. H. Moore, and J. P. Doering, Rev. Mod. Phys. **66**, 985 (1994).
[3] E. Weigold and I. E. McCarthy, *Electron Momentum Spectroscopy* (Kluwer/Plenum, New York, 1999).
[4] J. P. D. Cook, J. Mitroy, and E. Weigold, Phys. Rev. Lett. **52**, 1116 (1984).
[5] J. P. D. Cook, I. E. McCarthy, J. Mitroy, and E. Weigold, Phys. Rev. A **33**, 211 (1986).
[6] L. Frost, J. Mitroy, and E. Weigold, J. Phys. B **19**, 4063 (1986).
[7] J. Bonfert, H. Graf, and W. Nakel, J. Phys. B **24**, 1423 (1991).
[8] X. G. Ren, C. G. Ning, J. K. Deng, G. L. Su, S. F. Zhang, and Y. R. Huang, Phys. Rev. A **73**, 042714 (2006).
[9] Z. J. Li, X. J. Chen, X. Shan, X. X. Xue, T. Liu, and K. Z. Xu, Chem. Phys. Lett. **457**, 45 (2008).
[10] K. Liu, C. G. Ning, and J. K. Deng, Phys. Rev. A **80**, 022716 (2009).
[11] K. Liu, C. G. Ning, and J. K. Deng, Chin. Phys. Lett. **27**, 073403 (2010).
[12] K. Liu, C. G. Ning, Z. H. Luo, L. L. Shi, and J. K. Deng, Chem. Phys. Lett. **497**, 229 (2010).
[13] P. Pyykkö, Chem. Rev. **88**, 563 (1988).
[14] M. Pepper and B. E. Bursten, Chem. Rev. **91**, 719 (1991).
[15] W. Kutzelnigg, Chem. Phys. **225**, 203 (1997).
[16] W. J. Liu, M. Dolg, and L. M. Li, J. Chem. Phys. **108**, 2886 (1998).
[17] G. te Velde, F. M. Bickelhaupt, E. J. Baerends, C. Fonseca Guerra, S. J. A. van Gisbergen, J. G. Snijders, and T. Ziegler, J. Comput. Chem. **22**, 931 (2001).
[18] A. B. Cornford, D. C. Frost, C. A. Mcdowell, J. L. Ragle, and I. A. Stenhouse, J. Chem. Phys. **54**, 2651 (1971).
[19] W. R. Salaneck, R. W. Bigelow, H. J. Freund, and E. W. Plummer, Phys. Rev. **24**, 2403 (1981).
[20] G. Bieri, L. Asbrink, and W. Vonniessen, J. Electron Spectrosc. Relat. Phenom. **27**, 129 (1982).

[21] A. J. Yencha, M. C. R. Cockett, J. G. Goode, R. Donovan, A. Hopkirk, and G. C. King, Chem. Phys. Lett. **229**, 347 (1994).
[22] A. M. Grisogono, R. Pascual, E. Weigold, A. O. Bawagan, C. E. Brion, P. Tomasello, and W. von Niessen, Chem. Phys. **124**, 121 (1988).
[23] C. Lee, W. Yang, and R. G. Parr, Phys. Rev. B **37**, 785 (1988).
[24] H. Nakatsuji and K. Hirao, Chem. Phys. Lett. **59**, 362 (1978).
[25] H. Nakatsuji, Chem. Phys. Lett. **67**, 329 (1979).
[26] H. Nakatsuji, Chem. Phys. Lett. **177**, 331 (1991).
[27] C. G. Ning, S. F. Zhang, J. K. Deng, K. Liu, Y.-R. Huang, and Z.-H. Luo, Chin. Phys. B **17**, 1729 (2008).
[28] C. G. Ning, J. K. Deng, G. L. Su, H. Zhou, and X. G. Ren, Rev. Sci. Instrum. **75**, 3062 (2004).
[29] X. G. Ren, C. G. Ning, J. K. Deng, S. F. Zhang, G. L. Su, F. Huang, and G. Q. Li, Rev. Sci. Instrum. **76**, 063103 (2005).
[30] P. Duffy, D. P. Chong, M. E. Casida, and D. R. Salahub, Phys. Rev. A **50**, 4707 (1994).
[31] Y. Zheng, C. E. Brion, M. J. Brunger, K. Zhao, A. M. Grisogono, S. Braidwood, E. Weigold, S. J. Chakravorty, E. R. Davidson, A. Sgamellotti, and W. von Niessen, Chem. Phys. **212**, 269 (1996).
[32] E. van Lenthe, E. J. Baerends, and J. G. Snijders, J. Chem. Phys. **101**, 9783 (1994).
[33] ADF 2008.01 (SCM, Vrije Universiteit, Theoretical Chemistry, Amsterdam, The Netherlands, 2008).
[34] K. A. Peterson, B. C. Shepler, D. Figgen, and H. Stoll, J. Phys. Chem. A **110**, 13877 (2006).
[35] [https://bse.pnl.gov/bse/portal].
[36] M. J. Frisch *et al*., GAUSSIAN03, Revision E.01, (Gaussian Inc., Wallingford, CT, 2004).
[37] P. Pyykkö and H. Toivonen, *Tables of Representation and Rotation Matrices for the Relativistic Irreducible Representations of 38 Point Groups* (Abo Akademi, Abo, 1983), Vol. 43.
[38] P. Duffy, M. E. Casida, C. E. Brion, and D. P. Chong, Chem. Phys. **159**, 347 (1992).
[39] C. G. Ning, X. G. Ren, J. K. Deng, G. L. Su, S. F. Zhang, and G. Q. Li, Phys. Rev. A **73**, 022704 (2006).
[40] X. G. Ren, C. G. Ning, J. K. Deng, S. F. Zhang, G. L. Su, F. Huang, and G. Q. Li, Phys. Rev. Lett. **94**, 163201 (2005).
[41] J. Schirmer, L. S. Cederbaum, and O. Walter, Phys. Rev. A **28**, 1237 (1983).